

Helium line formation and abundance during a C-class flare

Vincenzo Andretta

*INAF - Osservatorio Astronomico di Capodimonte, Salita Moiariello 16, I-80131 Napoli,
Italy*

andretta@oacn.inaf.it

Pablo J. D. Mauas

Instituto de Astronomía y Física del Espacio, Argentina

Ambretta Falchi

INAF - Osservatorio Astrofisico di Arcetri, Italy

Luca Teriaca

Max-Planck-Institut für Sonnensystemforschung, Germany

ABSTRACT

During a coordinated campaign which took place in May 2001, a C-class flare was observed both with SOHO instruments and with the Dunn Solar Telescope of the National Solar Observatory at Sacramento Peak. In two previous papers we have described the observations and discussed some dynamical aspects of the earlier phases of the flare, as well as the helium line formation in the active region prior to the event. Here we extend the analysis of the helium line formation to the later phases of the flare in two different locations of the flaring area. We have devised a new technique, exploiting all available information from various SOHO instruments, to determine the spectral distribution of the photoionizing EUV radiation produced by the corona overlying the two target regions. In order to find semiempirical models matching all of our observables, we analyzed the effect on the calculated helium spectrum both of A_{He} (the He abundance) and of the uncertainties in the incident EUV radiation (level and spectral distribution). We found that the abundance has in most cases (but not in all) a larger effect than the coronal back-radiation. The result of our analysis is that, considering the error of the measured lines, and adopting our best estimate for the coronal EUV illumination, the value $A_{\text{He}} = 0.075 \pm 0.010$ in the chromosphere (for $T > 6300$ K) and transition region yields reasonably good matches for all the observed lines. This value is marginally consistent with the most commonly accepted photospheric value: $A_{\text{He}} = 0.085$.

Subject headings: Sun:activity — Sun:abundances — Sun:chromosphere

1. Introduction

A key ingredient to understand the physics of solar and stellar plasmas is their chemical composition. An astrophysical plasma is subject to chemical fractionation processes of diverse nature (gravity, thermal diffusion, etc., see e. g. Drake 2003) that can produce abundance “anomalies” between regions of different temperature and density. For the solar corona these anomalies are generally described in terms of the so-called FIP (*First Ionization Potential*) effect. Not only the details, but the very general physical framework behind this effect is still debated. However, one of the few aspects over which there is apparently a consensus, is that the FIP effect should arise in the chromosphere (Geiss 1982, 1998).

Helium is one of the few elements that exhibits strong lines forming in the chromosphere, and thus, in principle at least, its abundance ($[\text{He}/\text{H}] \equiv \log A_{\text{He}}$ (where $A_{\text{He}} \equiv N_{\text{He}}/N_{\text{H}}$, the ratio of number densities of He and H) could be estimated in that region. It is also the element with the highest FIP (24 eV). Furthermore, it is the second most abundant element in the Sun (and in the universe, for that matter), and therefore must be included in any theoretical model of fractionation processes in the solar atmosphere. Moreover, the coronal $[\text{He}/\text{H}]$ strongly depends on the availability of helium in the upper chromosphere (e. g.: Killie et al. 2005).

Unfortunately, analyzing helium lines in the solar atmosphere is a particularly challenging task, more so than other “typical” chromospheric lines such as $\text{H}\alpha$ or the Ca II H & K doublet. The main reasons are described in several papers (for example: Andretta & Jones 1997; Pietarila & Judge 2004). Among the problems that can be mentioned: all of its lines need detailed radiative transfer calculations; strong interlocking between $n = 2$ and $n = 3$ singlet and triplet levels makes the *simultaneous* treatment of EUV and optical lines almost unavoidable; the high excitation energies of all helium lines (a consequence of its high FIP value) makes those lines very sensitive to non-equilibrium effects; the ionization rates of neutral and ionized helium can be significantly affected by EUV radiation via the so-called “Photoionization - Recombination” (P-R) mechanism (e. g.: Zirin 1975; Andretta et al. 2003), and therefore not only coronal plasmas, but even the strong He II Ly- α at 30.4 nm can be significant photoionization sources for neutral helium (another example of the strong interlocking effects in the helium atomic system).

All these problems imply, among other things, that a realistic study of helium lines in the solar chromosphere requires quite sophisticated modeling, as well as simultaneous mea-

measurements in both the EUV and the optical (visible and IR) range. To this aim we planned an observing campaign (SOHO Joint Observing Programme 139) coordinated between ground based and SOHO instruments to obtain simultaneous spectroheliograms of the same area in several spectral lines, including four He lines (He I 58.76, He I 1083.0, He I 58.4 and He II 30.4 nm), that sample the solar atmosphere from the chromosphere to the transition region. The EUV radiation in the range $\lambda < 50$ nm and in the range $26 < \lambda < 34$ nm has also been measured at the same time.

In a previous paper (Mauas, Andretta, Falchi, et al. 2005, hereafter Paper II), we carried out an analysis of the helium line formation in a specific location of the observed active region (NOAA AR 9468, $\cos \theta = 0.99$), prior to a small two-ribbon flare (GOES class C1) developed in this region on 2001, May 26, around 16:00 UT. We found that the incident coronal radiation has a limited effect on the UV He lines (in partial agreement with the proxy-based analysis of Fredvik & Maltby 1999, of the He I 58.4 line), while being fundamental for the optical lines. For these lines, we also found that photons of shorter wavelengths are more effective at increasing their line depth. Incidentally, this latter finding implies that for the calculation of the He line profiles it is important, at least in principle, to correctly estimate not only the total number of ionizing photons, but also their spectral distribution. But the main result of Paper II was that the photospheric value of $[\text{He}/\text{H}]$ is compatible with our observations within an uncertainty of about a factor two and that such uncertainty could be reduced in a higher density regime.

On the basis of these results we decided to extend our analysis to the data taken during the flare. In this paper we present results of such analysis and study the formation of He lines after the main evaporation phase, when the He lines presumably originate in a high density plasma and the incident coronal radiation, larger than in the pre-flare phase, can be estimated with a lower uncertainty. We construct semiempirical models of the flaring atmosphere to match the observed line profiles from the chromosphere to the transition region, taking into account the total EUV irradiance in the range $\lambda < 50$ nm. We also analyze the effect of $[\text{He}/\text{H}]$ changes, with the purpose of attaining an empirical estimate of that parameter.

To this regard, we mention that techniques based on γ -ray line measurements produced in flares offer an alternative avenue for estimating the chromospheric He abundance (e. g. Mandzhavidze et al. 1997, 1999; Share & Murphy 1998). Results from these techniques seem generally to indicate an enhancement either of the accelerated α /proton ratio or of the “ambient” He abundance. Attempts at resolving this ambiguity seem however to hint that A_{He} is consistent with its accepted photospheric values (Murphy 2007).

For completeness, we should also mention recent EUV spectroscopic measurements of

A_{He} during a flare, made by analyzing the Balmer- γ of He II at 108.5 nm in off-limb spectra (Feldman et al. 2005), which yielded $A_{\text{He}} \sim 0.122 \pm 0.024$, marginally higher than the photospheric value. This result, however, refers to off-limb post-flare loops and thus cannot be directly compared with our on-disk, chromospheric measurements.

In Sec. 2 we briefly describe the set of observations, focussing our attention on two specific locations of the flaring region. In Sec. 3 we describe the procedures employed to estimate the incident coronal EUV radiation illuminating the regions under examination and in Sec. 4 the chromospheric modeling for those two locations. Finally, in Sec. 5 we explore how the helium spectrum is affected by the value of the chromospheric He abundance and by the uncertainties in the estimates of coronal radiation.

2. The Observations

A detailed description of the observing program is given in Teriaca, Falchi, et al. (2003) (hereafter Paper I). We recall here that spectroheliograms were acquired with the Horizontal Spectrograph at the Dunn Solar Telescope (DST) of the National Solar Observatory at Sacramento Peak in the chromospheric lines Ca II K, $H\alpha$, and Na I D as well as in the He I lines at 587.6 (D₃) and 1083 nm. The full field of view (FOV) of the DST, $170'' \times 170''$, was covered in about 5 minutes, with a sampling step of $2''$. Correcting for offsets among the different detectors resulted in a final useful FOV of $160'' \times 140''$ with an effective resolution of $2''$.

During the same period, spectroheliograms of the active region were obtained in selected spectral lines with the Normal Incidence Spectrometer (NIS) of the Coronal Diagnostic Spectrometer (CDS) (Harrison et al. 1995) aboard SOHO. The selected lines are: Fe XVI 36.1 nm in the NIS band #1; He I 58.4 nm, He II 30.4 nm (2nd order), O V 62.9 nm, and the blend Fe XII 59.26 + Fe XIX 59.22 nm¹ in the NIS band #2. The $4''$ -wide slit was stepped $6''$ covering a $148''$ wide area in ~ 5.5 minutes. The final useful FOV was $148'' \times 138''$ with an effective pixel size of $6'' \times 3''$.⁴ Ground-based and CDS data were aligned using SOHO/MDI images as a reference. We estimate the error around few arcseconds. CDS and ground based spectra are simultaneous within 2 minutes.

Another SOHO instrument, the Extreme ultraviolet Imaging Telescope (EIT; Delaboudinière et al.

¹In the case of the Fe XII 59.26+Fe XIX 59.22 nm blend, an analysis of the mean line wavelengths shows (see also Paper I) that the former contribution is small or even negligible in the areas interested by the flare, but, conversely, is dominant in the surrounding, unperturbed regions.

1995) provided synoptic series of full disk images centered on 17.1, 19.5, 28.4 and 30.4 nm around 13:00 and 19:00 UT, plus a series of full disk images centered on 19.5 nm acquired with a 12 minutes cadence during the routine *CME watch* program. Fig. 1 shows a few images extracted from the EIT 19.5 sequence, showing the development of the flare.

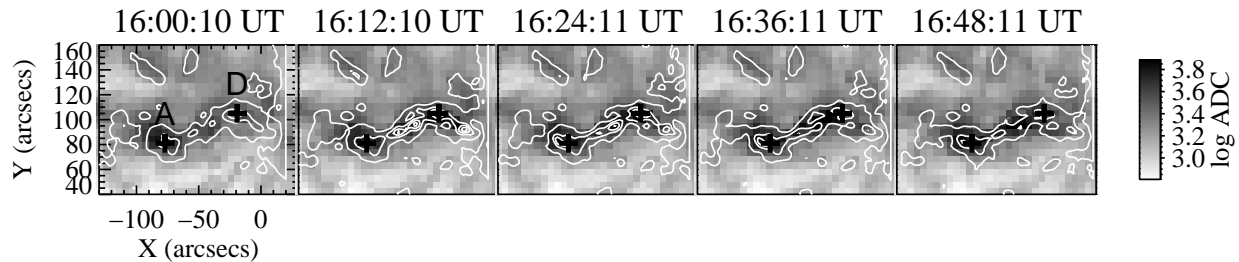


Fig. 1.— The evolution of the NOAA AR 9468 in the first hour of the event, as seen in the sequence of SOHO/EIT 19.5 nm images (see Fig. 2 for a comparison with XUV irradiance and $H\alpha$ radiance light curves). The contours represent $H\alpha$ isophotes relative to the DST raster scan nearest in time. The positions of the two regions studied in detail in this paper (regions A and D) are marked with crosses.

Finally, the EUV flux during the flare (see Figure 2) was observed by the Solar EUV Monitor (SEM) instrument aboard SOHO (Hovestadt et al. 1995). The CELIAS/SEM instrument provides calibrated total photon counts in the range $\lambda < 50$ nm (zero-th order, SEM₀), and in the range $26 < \lambda < 34$ nm (first order, SEM₁), at 1 AU.

The flare dynamics has been discussed in Paper I, where it has been shown that a large area of the flaring region is affected by chromospheric evaporation in a short time interval (16:02:30 - 16:05:30 UT) during the first impulsive phase. In the present paper we analyze the He line profiles after 16:13 UT, when the chromospheric evaporation is almost finished, in two distinct locations, which we term regions “A” and “D” (size of $4'' \times 2''$ each). These two regions are marked in Fig. 1

From what we obtained in Paper I, region A did not undergo any evaporation process, at least within our limit of detectability, while region D is in the area where we measured downflows at chromospheric levels and upflows at Transition Region (TR) and coronal levels. Moreover, while in region A the chromospheric radiance is almost constant after 16:13 UT, in region D it approximately follows the EUV light curve (see Figure 2) with a secondary maximum at about 16:20 UT, showing that also this small flare is a multiple event. A similar behaviour is also detected for the TR and coronal lines with temperatures up to 10^6 K.

We use region A as a control region where only small changes are detected in our observed features. We construct (Sec. 4) semiempirical models of the flaring atmosphere for

this region at two times when the SEM EUV irradiance is nearly the same: 16:14 and 16:33 UT (dashed lines in the SOHO/SEM light curve in the upper panel of Fig. 2).

For region D the models are constructed at 16:15, 16:20, and 16:35 UT (dotted lines). These times will be also referred to as t_1 , t_2 , and t_3 , respectively. Time t_2 corresponds to a peak of the total SEM irradiance, while at t_1 and t_3 the irradiances are almost equal. Therefore, the choice of these regions and times allows us to check whether and how the He I lines are influenced by the EUV coronal back-radiation, and/or by the atmosphere where they form. This point will be discussed more in detail in Sec. 3.1.

The two sets of optical line profiles are shown in Fig. 3, with the exception of the Na I doublet that did not change during the flare in the two considered regions. For region A, since the profiles remain practically unchanged, only the profiles observed at 16:14 are shown and compared with profiles taken in a nearby, relatively quiescent region, prior to the flare, which have been used to calibrate the spectra in absolute units.

The noise of individual spectra is sufficiently small to be negligible compared to the pixel-to-pixel variability within the target regions which, therefore, determines the uncertainty on the mean profiles. The uncertainties as function of wavelength on the mean profiles in region A at 16:14 UT and in region D at 16:20 UT are indicated in Fig. 3 as a grey band. In practice, those bands are obtained, at each wavelength, from the r.m.s. of the N profiles within the target regions, divided by \sqrt{N} .

It is important to realize that for the two relatively weak He I lines, the uncertainty in the central line depth (the quantity which carries most information about the chromosphere) is also due to the variability of the underlying photosphere. This fact is most evident in the continuum bands of the D₃ line at 58.76 nm. By examining the variability of the profiles normalized to the continuum, we estimate that for the latter line the photospheric variability contributes by about 50% to the variability of the central line intensity². In any case, the uncertainties shown in Fig. 3 for the two optical He I lines (of the order of 3%), are to be taken as upper limits for the uncertainties due to the variability of the chromosphere only.

In the case of the EUV He I lines, the width of the instrumental response of the CDS spectrograph prevents a detailed comparison of computed and observed line profiles. We thus considered only the radiances. For these lines, the main source of error is the uncertainty in

²We adopt here, as commonly done in Astrophysics, the term “specific intensity” or simply “intensity” in place of the more formally correct “spectral radiance” (SI units: $\text{W sr}^{-1} \text{m}^{-2} \text{nm}^{-1}$) and indicate it with the symbol I_λ ; with “radiance” it is then meant an intensity integrated over a wavelength band or a line profile: $\int I_\lambda d\lambda$ (SI units: $\text{W sr}^{-1} \text{m}^{-2}$). Finally, “irradiance” is the spectral and angular integral of an intensity: $\int I_\lambda d\lambda d\Omega$ (SI units: W m^{-2}).

the absolute radiometric calibration, estimated to be of the order of 30%.

3. Coronal back-radiation

In Paper II the average EUV illumination over the target area in active region AR 9468, integrated in the $\lambda < 50$ nm range, was computed using the spatial information provided by the EIT synoptic images to estimate the contribution to the full-disk SEM_0 0.1–50 nm irradiance due to the target region. This value, $I_{\text{ref}} = 1.2 \pm 0.2 \times 10^{15}$ photons $s^{-1} \text{ cm}^{-2} \text{ sr}^{-1}$, is considered here as the reference value. We recall that the emission from the He II lines has been subtracted from I_{ref} because these lines are taken into account in a self-consistent way in the model computations.

Following the same approach, and using the EIT 19.5 images as proxies, we estimated that, in the hour before the flare, the EUV radiation in regions A and D was, in average, about 2.2 and 1.6 times higher than I_{ref} . Since there are variations of the order of 30% in a 3×3 pixel box ($\approx 16'' \times 16''$) around the center of each region, the standard deviation of the *mean* value in the same box would be 3 times smaller. We however prefer to use the $3\text{-}\sigma$ value on the mean value quoted above, as it is large enough to encompass other possible sources of error (for instance those introduced by the use of EIT 19.5 images as proxy for the full 1-50 nm range). Thus, we estimated the EUV illumination over regions A and D to be, respectively, about 2.6×10^{15} and 1.9×10^{15} photons $s^{-1} \text{ cm}^{-2} \text{ sr}^{-1}$ (Table 1).

The implicit assumption in such an approach, as explained in Paper II, is that the spectral distribution of the EUV radiation over the active region does not change significantly. For the observations taken during the flare, however, this assumption may not be valid. Thus, we adopted an altogether different approach for estimating the EUV illumination at the times of our observations.

From the EIT sequence of images we can estimate that the only event that can cause the increase in EUV irradiance shown in the topmost panel of Fig. 2, is the C-class flare we observed. From the *increase* in SEM irradiance, Δf , and from the knowledge of the angular area affected by the flare, $\Delta\Omega$, we can then estimate the *increase* in radiance in the flaring region, $\Delta I = \Delta f / \Delta\Omega$. The total radiance in the region is then obtained by adding to ΔI the estimates of the pre-flare average radiances given above.

For a first, rough estimate, we can start from a visual determination, from Fig. 2, of the excess irradiance in the SEM_0 measurements due to that event: $\Delta f \approx 2$ to 4×10^8 photons $s^{-1} \text{ cm}^{-2}$ in the first 60 minutes of the event. On the other hand, from both EIT and CDS observations, we estimate flare areas to be of the order of $\Delta\Omega \approx 1500$ to $2000('')^2$ in the

same time interval . Consequently, we expect radiances in the flaring regions to increase by something of the order of $\Delta I \approx 6$ to 8×10^{15} photons $\text{s}^{-1} \text{cm}^{-2} \text{sr}^{-1}$.

The inaccuracy of this estimate is mainly due to the approximate definition of the flaring area: it can vary by as much as a factor 2 or 3, depending on which spectral signature is considered. For a more precise determination of the excess irradiances in regions A and D, we refined the method by using the information given by the variation in time (light curves) *above the pre-flare mean value* of both the SEM irradiance and of the observed spectral signatures in our data set. More in detail, we proceeded as follows:

Step #1: We created a set of reference images, both from CDS and from EIT, by averaging the (co-aligned) images in the 40 minutes preceding the onset of the event. The variability of these images around the average is of the order of 0.1–0.2% (standard deviation), or even less.

Step #2: We obtained maps of “residual” or “excess” radiance in each spectral feature during the flare, $\Delta I_{ij}^k(t_h)$, by subtracting the reference pre-flare images (taking into account solar rotation) for each time t_h , and for each pixel (i, j) . Multiplying by the pixel angular size, $d\omega^k$, we then obtain the contribution of each line and of each pixel to the EUV irradiance, $\Delta f_{ij}^k(t_h) = \Delta I_{ij}^k(t_h) d\omega^k$. The result is shown in Fig. 4 for CDS images only. A similar procedure has been applied to the EIT sequence as well. More details on the analysis of the individual CDS rasters can be found in Paper I. Here we only mention that the rasters were taken by moving the slit from W to E — right to left, in the images of Fig. 4, where the beginning of each raster is indicated at the top of the corresponding column.

Step #3: We computed the light curves of the *excess* irradiance for each spectral feature by summing the contributions $\Delta f_{ij}^k(t_h)$. Each curve represents the contribution of the considered feature to the EUV excess irradiance during the flare, under the assumption that no other significant event is occurring on the solar surface outside the CDS FOV. We verified the correctness of that assumption by inspecting the full-disk EIT 19.5 images during the event. The resulting light curves are shown in the top panel of Fig. 5. The set of CDS and EIT curves cover a broad range of temperatures (from $\log T < 5.0$ for He I and He II, to $\log T \sim 6.9$ for Fe XIX), and can thus be regarded as a good set of proxies for the temporal and spatial evolution of the various temperature components of the flaring plasma.

Step #4: We found a linear combination of those light curves matching reasonably well the evolution of SEM_0 measurements during the flare. More in detail, we modeled the total *excess* irradiance at each time t_h , $\Delta f(t_h)$, with a linear combination of the *excess* irradiance

of each line k , in the form:

$$\Delta f(t_h) \approx a_0 + a_1 t_h + \sum_k b_k \sum_{ij} \Delta f_{ij}^k(t_h) . \quad (1)$$

The term $a_1 t_h$, that accounts for possible overall changes in the active region structure (hence: of the overall EUV emission) in the course of the event, is actually rather small: To reduce the number of free parameters, we set this term to zero.

The two resonance helium lines, He I 58.4 and He II 30.4, exhibit an almost identical behaviour: only the latter has been taken into account in the linear regression.

The comparison of the thus modelled EUV SEM irradiance (grey line in Fig. 5) with the actual measured signal (smoothed to account for the 5-minutes duration of the CDS rasters) is shown in the bottom panel of Fig. 5, for the first ≈ 120 minutes of the event. We stress that $b_k \sum_{ij} \Delta f_{ij}^k$ is *not* the contribution of the individual line k to the EUV irradiance, but is instead the contribution of the *group* of lines of similar temperatures, for which line k is a proxy.

Beyond the mere application of the mathematical linear regression procedure, we think useful to remark here how the different parts of the irradiance SEM light curve are due to different temperature contributions of the flare plasma. More specifically, the first peak, at the time resolution of the CDS rasters, is modelled essentially by the cooler temperature lines (proxies: He II and O V), while the second peak (at $\sim 16:20$ UT) is due mostly to the hottest flaring plasma (proxy: Fe XIX), with a tail modelled by progressively cooler components (Fe XVI and then EIT 19.5). These findings, based on the modelling of the SEM₀ light curve, are qualitatively consistent with the characteristics of the other irradiance curves shown in Fig. 2: the second peak is indeed absent in SEM₁, while is more pronounced in the GOES signal.

Step #5: The coefficients of the linear combination, b_k , were then applied to the corresponding residual images on a pixel-by-pixel basis, producing a map of the contribution to the total *excess* EUV irradiance in the SEM spectral range ($\lambda < 50$ nm) as function of time during the flare. The contribution due to transition region and coronal lines (henceforth, for brevity: “the coronal component”), needed in the model calculations, is obtained by subtracting the contribution of the proxy He II 30.4 nm, that will be computed self-consistently in the models. Thus, the contribution of each pixel to the EUV coronal irradiance, divided by the pixel’s angular size, yields an estimate of the spatial variation of coronal radiance *enhancement*, in the band $\lambda < 50$ nm, over the flare area. The result of such a procedure is shown in Fig. 6.

If we make the reasonable assumption that the EUV emission during the flare is optically

thin, the maps of EUV *excess* radiance of Fig. 6 are also maps of EUV back-radiation illuminating the chromosphere. In Sec. 3.1 we will discuss more in detail this assumption.

Step #6: Finally, by adding the pre-flare, average value of radiance estimated in the two target regions, A and D, we obtained an estimate of the value of EUV radiance of coronal origin in the band $\lambda < 50$ nm, I_{cor} , as function of time over the two target regions, and in particular at the times of the optical observations of Fig. 3 (Table 1).

Region	Time (UT)	Coronal radiance		
		Excess	Total	Total/ I_{ref}
A	pre-flare	—	2.6	2.2
	16:14	0.38	3.0	2.5
	16:33	1.73	4.4	3.6
D	pre-flare	—	1.9	1.6
	16:16	5.48	7.3	6.2
	16:20	7.38	9.2	7.7
	16:35	5.25	7.1	6.0

Table 1: Coronal radiances for regions A and D, in units of 10^{15} photons $\text{s}^{-1} \text{cm}^{-2} \text{sr}^{-1}$. The value $I_{\text{ref}} = 1.2 \times 10^{15}$ is the reference (average pre-flare) value for the target area, estimated in Paper II.

The (statistical) uncertainties in the excess number of photons are of the order of $\approx 0.4 \times 10^{15}$ (region A) and $\approx 2 \times 10^{15}$ (region D) photons $\text{s}^{-1} \text{cm}^{-2} \text{sr}^{-1}$, estimated as the $3\text{-}\sigma$ variation of the illumination around the target regions.

We have also explored the systematic variations induced by changing the most relevant parameters that could affect the result of the procedure described above (for example: using a constant instead of a linear background in the regression calculations of Step #4); the resulting overall variations are smaller than the statistical uncertainty at the $3\text{-}\sigma$ level quoted above.

Together with the uncertainty in the pre-flare radiance enhancements estimated earlier in this section ($\approx 30\%$), and with the uncertainty of I_{ref} estimated in Paper II (0.2×10^{15} , or about 17%), we thus obtain an overall uncertainty in the total coronal radiance of the order of 25% to 35% in both regions A and D.

3.1. The spectral and angular distribution of the coronal back-radiation

In Paper II we estimated the spectral distribution of the coronal photoionizing EUV radiation by taking a reference spectral distribution, and multiplying that distribution by a factor (close to unity) such that the radiance in the range $\lambda < 50$ nm equals $I_{\text{ref}} = 1.2 \times 10^{15}$ photons $\text{s}^{-1} \text{cm}^{-2} \text{sr}^{-1}$.

In that paper we adopted as our reference spectral distribution the one for a “typical” active region computed with the spectral code and atomic database CHIANTI version 4 (Young et al. 2003). The CHIANTI calculations require a description of the density and temperature distribution in the atmosphere via the Differential Emission Measure (DEM), defined as $N_{\text{H}}N_{\text{e}}(dT/dh)^{-1}$, where h is a coordinate along the line of sight; we adopted the table in file `active_region.dem` provided with the package, which is based on data from Vernazza & Reeves (1978). Furthermore, we adopted a “hybrid” set of abundances (intermediate between photospheric and coronal elemental mixtures: Fludra & Schmelz 1999), and a constant pressure of $P_e/k = 3 \times 10^{15} \text{cm}^{-3} \text{K}$. We verified that the use of the more recent version 5 of the same code (Landi et al. 2006) did not alter significantly that reference spectral distribution (Fig. 1 of Paper II).

In the case of the flaring atmosphere we are considering, however, it is possible that significant changes in the spectral distribution may occur. We tested this possibility by considering the case where departures from the “standard” spectral distribution (the pre-flare AR EUV spectrum, in fact) could be more pronounced: the emission above region D at 16:20 UT, where we observe a peak of total EUV emission (Table 1), as well as a peak in the hot Fe XIX line (Fig. 5).

To do so, we found a DEM producing the measured total number of photons in the range $\lambda < 50$ nm (9.2×10^{15} photons $\text{s}^{-1} \text{cm}^{-2} \text{sr}^{-1}$), and giving at the same time a reasonable match to the transition-region and coronal lines observed by CDS: O V 62.9 nm, Fe XVI 36.1 nm, and the blend Fe XII 59.26+Fe XIX 59.22 nm. The optically thick helium lines have not been considered in this analysis, but are nonetheless shown in the plots summarizing the results of this test (Fig. 7).

In the calculations, we assumed a higher pressure, $P_e/k = 3 \times 10^{16} \text{cm}^{-3} \text{K}$, than in the pre-flare atmosphere. This value of the pressure corresponds, for instance, to $N_e \approx 10^{11}$ and $\approx 10^{10}$ at $\log T = 5.5$ and 6.5 respectively. These densities are generally consistent with flare densities found in the literature (e. g.: Dere & Cook 1979), although lower densities have sometimes been reported (Cook et al. 1994). Aside of the overall scale factorized by the DEM, the specific value for P_e/k affects only the relative radiances of the density-dependent lines, and thus it is of little importance for the purpose of estimating the *global* flare spectral

distribution for $\lambda < 50$ nm.

Such a DEM is compared in the left-hand panel of Fig. 7 with the DEM used to compute the pre-flare, reference spectrum. The corresponding observed line radiances are shown in that panel multiplied by the factor $\text{DEM}(T_{\text{eff}})/I_{\text{calc}}$ (as in, e. g., Del Zanna et al. 2002); here T_{eff} is the temperature of peak line emission. The error bars in the case of the data taken during the flare reflect the statistical variability in the 9 pixels around and above the target (D) region. Thus, we do not show the theoretical uncertainties or the calibration uncertainties both on the absolute intensities and on the CDS NIS1/NIS2 relative radiances (i. e.: the radiance of the Fe XVI line relative to all the others).

The DEM-derived pre-flare and the flare spectra are compared in the right-hand panel of the same figure (dark and light grey histograms, respectively). We also show the pre-flare “standard” spectrum multiplied by the factor required to obtain the same total number of photons below 50 nm as in the flare spectrum (dashed histogram). The largest differences between these two spectra occur in the region below 15 nm, where the number of photons in the modelled flare spectrum is about a factor 4 higher than in the AR scaled spectrum. Conversely, the number of photons in the range 15–50.4 nm is about 20% smaller than in the AR scaled spectrum.

On the other hand, for both distributions the bulk of the photoionizing photons is in the range $15 < \lambda < 50$ nm (about 3/4 of the total). In fact, this is the main reason why, as discussed in Paper II, the shorter wavelength part of the spectral distribution has relatively little effect on the photoionization of helium: We found that only the He I 1083 line shows small changes due to the different penetration depths in the chromosphere of the EUV photons of different energies. We will further discuss this point in Sec. 5.2.

In conclusion, we expect, and indeed find (see Sec. 5.2), that for our calculations it is not necessary to take into account the details of the distribution of photon energies: after all, we are studying a quite small flare. We thus simply scaled the “standard” spectral distribution by the appropriate factors listed in the last column of Table 1.

Concerning the problem of the angular distribution of the EUV photoionizing photons, we have already showed in Paper II that, despite their relatively featureless spatial distribution across the target AR prior to the flare, at the chromospheric depths the details of the angular distribution are relatively unimportant compared to the overall spectral distribution and, most importantly, to the total number of impinging photons.

In the case considered in this paper, on the other hand, during the flare the EUV emission is clearly concentrated in smaller areas (Figs. 4 and 6). It is therefore reasonable to assume that the main sources of ionizing radiation are concentrated directly above, or

very near the target regions. We verified this assumption using the control region (region A): during the time span we are considering, the helium lines in that region hardly change (Fig. 3), despite the large variations of the EUV radiation around (above) region D (see Table 1), which is roughly 40 Mm away. So, it is clear that the flaring chromosphere in region A, and *a fortiori* in region D, is sensitive only to the EUV radiation coming from regions significantly closer than $40 \text{ Mm} \approx 50''$, or, in other terms, is sensitive to the radiation coming at most from a few EIT or CDS pixels away.

4. Chromospheric modeling

Once the coronal back-radiation has been determined, semi-empirical models were constructed to match the observed profiles. The modeling was done using the program PANDORA (Avrett & Loeser 1984). Given a T vs. h distribution, we solved the non-LTE radiative transfer and the statistical and hydrostatic equilibrium equations, and self-consistently computed non-LTE populations for 10 levels of H, 29 of He I, 15 of Fe I, 9 of C I, 8 of Si I, Ca I and Na I, 6 of Al I and He II, and 7 of Mg I. In addition, we computed 6 levels of Mg II, and 5 of Ca II. The atomic models we used for H and Ca II are described in Mauas et al. (1997) and Falchi & Mauas (1998). The models we used for He I and He II are described in Paper II. More details on the modeling, and on the different assumptions and their validity can be found in Falchi & Mauas (1998) and in Paper II. The adopted microturbulence, in particular, is the same as in the latter work.

The modeling was done in a plane-parallel atmosphere. This is certainly an adequate approximation if we consider the much larger horizontal size of the target areas (several thousands of km) compared with the thickness of the chromosphere under study (a few hundred km). The effect of a possible filamentary structure of the atmosphere is however much more difficult to assess.

The only (qualitative) assessment we can make, from a radiative transfer point of view, is that photons could perhaps escape more easily from a set of randomly oriented, high-density structures embedded in a lower density medium than from a homogeneous atmosphere, especially in the case of high density contrast and of a sparse distribution of the filamentary structures. Thus, we may expect some modifications in the details of the profiles of the more optically thick lines: for instance, a reduction of the depth of self-reversed cores, if present. We may also expect that (effectively) optically thin lines should be least affected by atmospheric inhomogeneities.

In the case of more ordered, more closely packed, and thicker structures on the other

hand, the outcome could be somewhat different, as shown by Gunár et al. (2007), who studied the formation of the hydrogen Lyman lines in prominences, modelled as a set of parallel, finite slabs (“threads”), each 1000 km wide: each one, that is, as wide as the entire chromosphere we are modelling (Figures 8 and 11). We remark, however, that even in such a relatively extreme case, the changes are typically not very dramatic, and observable only at high spectral resolution.

In any case, there is little or no information, to our knowledge, on the effect of a flare on the chromospheric fine structure. Thus any more precise assessment on the effect of non-uniformity on the emerging profiles is virtually impossible at this stage.

In Fig. 3 we have shown the sets of optical profiles used in the modeling procedure. Since different features of the lines are sensitive to modifications in different parts of the chromosphere, the models were constructed following several steps. First, we fixed the deepest part of the atmosphere by matching the wings and the K_1 minimum of the Ca II K line, which are formed in the high photosphere and the temperature minimum region.

As a second step, we modified the chromosphere and the lowest part of the transition region until a satisfactory match was found for the profiles of $H\alpha$, Ca II K, and He I 1083 and 587.6. We recall that the profiles of the first two lines do not depend on the coronal back-radiation field.

The profiles of the two helium lines are formed in two distinct regions: most of the radiation is originated in the photosphere, which in the quiet Sun results in a weak absorption line at 1083 nm, and no noticeable line at 587 nm. However, already in the active region studied in Paper II we found that there is an important chromospheric contribution. This contribution becomes, of course, much more important in the flaring atmospheres we are studying here, and depends not only on the thermal structure of the high chromosphere and the low transition region, between 10^4 and 2.5×10^4 K, but also on the coronal EUV incident radiation.

Finally, both ultraviolet lines, the He I line at 58.4 nm and the He II line at 30.4 nm, depend on the structure of the low and mid-transition region, from 3×10^4 to 5×10^4 K for the 58.4 line, and up to 1×10^5 K for the 30.4 line. As a third step, therefore, we modified the structure of this region to obtain a good match for the line fluxes of these UV lines, measured with SOHO/CDS. Generally, it was necessary to iterate between steps 2 and 3 before a final model was obtained.

We first computed models for regions A and D, marked in Fig. 1, using the coronal radiation determined in Sec. 3 and the same value of the helium abundance ($A_{\text{He}}=0.1$) we used in Paper II. The resulting computed intensity profiles were convolved with the

appropriate instrumental response.

4.1. Modeling of region A

For region A, where the observed lines do not change during the considered time interval, we obtained the model shown in Fig. 8, which gives a good match between the observed and computed lines. In the same figure, we also show, for the line cores, the intensity contribution functions, defined as $dI/dh = S \exp(-\tau)\chi$, where I is the intensity, h is the height in the atmosphere, S , τ and χ are, respectively, the source function, the optical depth, and the opacity in the line core.

The observed and computed profiles of the lines formed essentially at chromospheric levels are shown in Fig. 9. The bars in the Figure indicate the uncertainty of the observed profiles (see also Fig. 3). It can be seen that the agreement found is very good, well within the error bars, in all cases. In the case of the optical He I lines, however, we recall that, as discussed in Sec. 2, the error bars in the line centers also include the effect of variations of the underlying photosphere within the target region, and therefore represent an upper limit to the variation induced by chromospheric changes.

It can also be seen that only the He lines are affected by the EUV radiation, and that the computed profiles agree with the observations within the range of variability in the target region for both values of the coronal radiation indicated in Table 1.

We have already mentioned in Sec. 2 that the UV lines (the He I 58.4 and the He II 30.4) have a large width due essentially to the instrumental profile: therefore the comparison with the models can be done only through the radiances, which are shown in Table 2. It can be seen that it is possible to obtain line radiances in good agreement with the observed ones using the same atmosphere, despite the variation of the coronal radiation of about 50% during the considered time interval (see Sec. 3 and Table 1).

We remark here that the temperature structure in the region of formation of the He II 30.4 nm line is not constrained by other lines. Thus, for the remainder of the discussion, we will not consider a match of the He II Ly- α to be a significant constraint on the atmospheric parameters.

4.2. Modeling of region D

For region D, where the chromospheric intensity (Fig. 2) approximately follows the EUV light curves, we were able to find models reasonably matching the observations at t_1 and t_3 , but it was not possible to obtain a model that would simultaneously reproduce all the profiles observed at t_2 .

In particular, the radiances of the He I 58.4 line always results considerably higher than the observed one if we match the profiles of the other lines, and in particular of $H\alpha$. Conversely, it is possible to find models that reproduce the radiance of the resonance He I line, but in this case the other lines, in particular $H\alpha$, are poorly fitted. It should be kept in mind that it is precisely at this time when the regions of formation of the 58.4 line and of $H\alpha$ overlap most, and therefore the model is best determined (see Sec. 5.1).

5. Discussion

In order to find in region D a model of the flaring atmosphere that matches all the observed lines during the considered time interval, and in particular that matches *both* $H\alpha$ and He I 58.4, we explored the two aspects that most likely affect the helium spectrum: the chromospheric helium abundance, A_{He} (Sec. 5.1), and the spectral distribution and overall level of EUV coronal back-illumination (Sec. 5.2).

5.1. The effect of helium abundance

To explore the effect of the helium chromospheric abundance, we computed a series of models for kernel D at t_2 , using values of $A_{\text{He}}=0.085, 0.075, 0.065,$ and 0.055 for $T > 6300$ K, i. e. in the atmospheric layers that strongly contribute to the formation of the considered lines. Since a change in the helium abundance affects the hydrostatic equilibrium, models with the same T vs. h structure but different abundances give, in principle, different emitted profiles not only for the He lines, but for all the other chromospheric lines as well, and for $H\alpha$ and the Ca II lines in particular. Therefore, for each value of A_{He} we had to compute a different model.

In Fig. 10 we show the computed radiance of the 58.4 He line and the central intensity of the D₃, 1083 and Ca II K lines, for the best-matching models for every value of the assumed A_{He} . The observed values and their uncertainties, as described in Sec. 2, are also shown. The variations of $H\alpha$ around the mean value of its central intensity are of the same order as

the analogous variations of the Ca II K line, and thus are not shown in Fig. 10.

The Ca II K and the He I 1083 lines depend very weakly on A_{He} , in the sense that, for each value of A_{He} , it was possible to find a model matching the observed profiles within the errors.

On the contrary, the He I D₃ and 58.4 lines strongly depend on A_{He} : the 58.4 radiance is higher than the observed value (beyond the error bar) for $A_{\text{He}} = 0.1$, and quickly decreases for smaller values of A_{He} , crossing the mean observed value at $A_{\text{He}} \sim 0.07$. On the other hand, the D₃ central intensity increases with decreasing A_{He} , and for A_{He} smaller than ~ 0.075 significantly exceeds the observed value. In practice, the D₃ central intensity approaches the photospheric continuum, i. e. the line *disappears*, for $A_{\text{He}} < 0.05$.

In other words, both the He I D₃ and 58.4 nm lines become in fact *weaker* as A_{He} decreases. This result may appear obvious after a superficial analysis neglecting the non-linearity of non-LTE problems. In fact, the He I 1083 nm line does not display the same behaviour: over the range of abundances explored, it was nearly always possible to find a temperature structure fitting both that line and the other chromospheric lines – with the exception of the lowest value, $A_{\text{He}}=0.05$.

Considering the error of the measurements, we believe that $A_{\text{He}} = 0.075$ is the best compromise that allows reasonably good matches for all the considered lines. We notice that a variation of $\pm 14\%$ of A_{He} (i. e.: $0.65 \leq A_{\text{He}} \leq 0.85$) still allows a good match between observed and computed lines within the error of the observations.

With this value of A_{He} , we also determined the models for region D at t_1 and t_3 UT, which are shown in Fig. 11. The same figure also shows, for the line cores, the intensity contribution functions for the model corresponding to the second maximum of EUV emission, at t_2 .

A comparison between observations and calculations for the three models is shown in Fig. 12. The bars in the Figure indicate the uncertainties of the observed profiles. It can be seen that the agreement found is very good, well within the errors, with the same caveat regarding the error bars of the optical He I lines discussed in Sec. 4.1. The computed radiances for the UV lines are compared with the observation in Table 2. Also in this case, the agreement is well within the errors in the observations.

5.2. The effect of coronal illumination

In the discussion on the effect of A_{He} on our calculations, we have assumed the values of I_{cor} given in Table 1. Those values, however, have an uncertainty of about 30%, as

Region	Time (UT)	He I 58.4 nm		He II 30.4 nm	
		Obs.	Comp.	Obs.	Comp.
A	16:14	2.65	2.77	16.0	15.3
	16:33	2.65	2.91	16.0	14.0
D	16:15	4.34	4.35	32.7	31.5
	16:20	4.93	5.29	24.0	22.9
	16:35	3.24	3.32	14.6	15.4

Table 2: Observed and computed radiances for the He UV lines. Units of 10^4 ergs s^{-1} cm^{-2} sr^{-1} .

estimated in Sec. 3. Moreover, the spectral distribution of the photoionizing photons is also somewhat uncertain. To assess how these uncertainties affect the profiles of the helium lines, we performed a set of calculations for Kernel D at t_2 , since it corresponds to the second emission peak (after the initial impulsive peak), when the differences with the situation studied in Paper II are the largest.

To test the effect of the uncertainty in the overall coronal back-illumination, we computed the He profiles increasing and decreasing by the $\approx 30\%$ estimated uncertainty (Sec. 3) the value listed in Table 1, for the models with $A_{\text{He}}=0.1, 0.085, 0.075$. The results of this tests are synthetically shown in Fig. 10 by thin error bars: higher values of I_{cor} produce stronger He I lines (deeper optical lines, and higher radiances in the EUV line).

For $A_{\text{He}}=0.1$, we found that the computed radiances of the He I 58.4 nm line change very little. In fact, a change in I_{cor} much larger than 30% (which, we recall is a “safe” 3σ value) would be required to match this radiance within the error bar of the observed value.

For $A_{\text{He}}=0.075$, for which we obtained the best overall fit (Sec. 5.1) we found that modifying the value of I_{cor} by 30% does indeed produce significant changes in the calculated profiles. It appears, in this case, that the lower value of A_{He} increases the penetration depth of EUV coronal photons, towards regions where the P-R mechanism effectively competes with collisional processes in the formation of the helium spectrum, even of the EUV resonance He I line.

To assess to what extent the uncertainty in the spectral distribution of EUV coronal photons can affect the results described in Sec. 5.1, we computed the He I profiles using the DEM-derived flare spectral distribution described in Sec. 3.1, for the cases with $A_{\text{He}}=0.1, 0.085, 0.075$. The results are indicated in Fig. 10 with open dots.

It can be seen that the changes are small, well within the error of the observations. We

can therefore exclude that the discrepancy between calculations and observations in the case of $A_{\text{He}}=0.1$, noted in Sec. 4.2, can be due to the uncertainty in the photoionization radiation.

In order to explore more systematically the effect of the spectral distribution of the photoionizing radiation, we also performed tests similar to the ones included in Paper II, considering for the spectral distribution different step functions, which are non-zero only in a limited spectral range, and zero outside it. The wavelength ranges we considered for this tests are: 2.5 – 5.0 nm, 5 – 10 nm, 10 – 20 nm, 20 – 30 nm, 30 – 40 nm and 40 – 50.4 nm.

In Fig. 13 we show the intensity in the center of the 1083 line and the radiance of the 58.4 line, as a function of I_{cor} . We do not show the central intensity of the D₃ line, since its behavior is very similar to the one of the 1083 nm line. We note that in Paper II we limited our tests to EUV radiances $I_{\text{cor}} < 3 \times 10^{15}$ photons s⁻¹ cm⁻² sr⁻¹, whereas here we extended the tests to 1.2×10^{16} .

Several important conclusions can be drawn from this figure. First, the effect is different on the two lines: the central intensity of the 1083 line is most sensitive the harder extreme of the spectrum (down to the threshold of 2.5 nm), while the reverse is true for the radiance of the 58.4 nm line, which is dominated by the longer wavelength bands and it is also nearly insensitive to photons below 10 nm.

For the 1083 and the D₃ lines the relevant parameter, as in the case discussed in Paper II, is the ratio between the helium and hydrogen photo-ionization cross sections, which in the band 0.5–10 nm is 3 to 5 times larger than at 50 nm. Therefore, coronal photons at larger wavelengths are absorbed before they reach the chromospheric heights where these lines are formed. Since, as we explained in Paper II, the ratio between the He I and H cross sections changes slowly at long wavelengths, the details of the spectral distribution between 20 and 50.4 nm are of little relevance for the resulting 1083 nm central intensity.

While these results are qualitatively consistent with those of Paper II, the effect of the shortest wavelength photons (in the band 2.5–5.0 nm) is remarkably different. While that band had practically no effect on the He I 1083 line computed in the AR model discussed in Paper II, we found that, in this flaring atmosphere, these photons may have a role in the formation of that line.

The reason for the difference lies in the higher temperature and densities of the model chromosphere of region D: the He I 1083 forms in a region where most neutral or singly-ionized metals, whose inner-shell absorption cross sections would otherwise dominate the opacity in that band, have already mostly disappeared.

The He I 58.4 nm line, on the other hand, is formed higher in the transition region,

where most hydrogen is ionized, and therefore in this case the relevant parameter is the helium photo-ionization cross section alone, which is larger close to the continuum head, at 50.4 nm.

Note that, by contrast with the situation studied in Paper II, in this case the much larger coronal radiation has some effect on the radiance of the He I UV line, for A_{He} up to 0.1 (Fig. 10). The He II UV line, on the other hand, which forms at higher temperatures, is not affected by the coronal radiation, as was the case for the active region prior to the flare (see Paper II).

6. Conclusions

During a small two-ribbon flare, we obtained simultaneous and cospatial observations, including the chromospheric lines Ca II K, H α and Na I D as well as the He I lines at 587.6 (D₃), 1083 and 58.4 nm and the He II line at 30.4 nm. The EUV irradiance in the ranges $\lambda < 50$ nm and $26 < \lambda < 34$ nm has also been measured at the same time.

We analysed the formation of the He lines after the first impulsive burst of the flare, i. e. after 16:13 UT, in two different locations of the flaring area, named A and D. In region A the chromospheric radiance is almost constant during the time interval we considered, while in region D it approximately follows the EUV light curve with a maximum emission at about 16:20 UT (Fig. 2). A similar behaviour is also detected for the TR and coronal lines with temperatures up to 10^6 K. We determined the incident photoionizing EUV radiation produced by the corona overlying the target regions, by using information from various SOHO instruments (imagers and spectrographs) and we concluded that in region A the variability of coronal radiance during the flare is less than a factor 2, while in region D is about a factor 5 (Table 1).

We determined the spectral distribution of the coronal radiation over the region D at 16:20 UT, where we observe a peak of total EUV emission, as well as a peak in the hot Fe XIX line (Fig. 5). We found that the largest differences between the pre-flare and the flare spectrum occur in the region below 15 nm.

These differences, however, are not large enough to compensate for the overwhelming contribution of longer wavelength photons to the total EUV photoionizing emission in this relatively small flare. We therefore simply scaled the spectral distribution of a “typical” active region by the appropriate factors listed in the last column of Table 1. With this coronal radiation, we built semiempirical atmospheric models trying to match our set of observables for regions A and D, using the same value of the helium abundance ($A_{\text{He}}=0.1$)

we used in Paper II. The He lines and continua are self-consistently computed in the radiative transfer calculations.

For region A we were successful in obtaining line spectral intensities and radiances in good agreement, within the errors, with the observed ones at the considered times, using a constant atmosphere and the coronal radiations determined in Sec. 3. Taking into account that the formation of the helium lines in this case still falls in a regime where the P-R mechanism is important (Fig. 9), this result makes us confident that our assumptions for the coronal radiation and its spectral distribution are acceptable.

For region D, we were able to find models producing profiles reasonably matching the observations at 16:15 and 16:35, but it was not possible to obtain a model capable of simultaneously reproduce all the profiles observed at 16:20, when the flare emission is maximum. In particular, it was not possible to simultaneously match $H\alpha$ and the He I 58.4 line. We therefore explored the two aspects that most likely can have an effect on our calculations: the chromospheric helium abundance, A_{He} (Sec. 5.1), and the spectral distribution and overall level of EUV coronal back-illumination (Sec. 5.2).

Since a change in the helium abundance affects the hydrostatic equilibrium, for each considered value of A_{He} we had to compute a different model. We used values of $A_{\text{He}}=0.085$, 0.075, 0.065 and 0.055 for $T > 6300$ K and we showed that the He I D_3 and 58.4 lines strongly depend on A_{He} , both becoming weaker as A_{He} decreases. In particular the D_3 line disappears for $A_{\text{He}} < 0.05$, setting a lower limit for the A_{He} value. On the contrary, over the range of abundances explored, it was always possible to find an atmospheric structure matching He I 1083 and the other chromospheric lines. Taking into account the error of the measured lines, we regard $A_{\text{He}} = 0.075$ as the best compromise that allows reasonably good matches for all the considered lines and we found that a variation of ± 0.010 (or: $\pm 14\%$) of A_{He} is still acceptable within the error of the observations, *with the average value of coronal illumination determined in Sec. 5.2*.

On the other hand, an analysis of the effect of the coronal illumination *at a given value of* A_{He} (in Sec. 5.2 we considered $A_{\text{He}}=0.1$, 0.085 and 0.075) led us to exclude that uncertainties in the determination of this parameter could be responsible for the discrepancies at $A_{\text{He}}=0.1$.

We also determined new models for region D at 16:15 and 16:35 UT using $A_{\text{He}}=0.075$. Thus, for these two times we have models matching all the observations for both $A_{\text{He}} = 0.075$ and $A_{\text{He}} = 0.1$. In these cases, as in the case of Region A (Sec. 4.1) the incomplete overlap between the formation regions of $H\alpha$ and He I 58.4 (see for instance Fig. 8) does not allow a determination of A_{He} with an uncertainty better than a factor of two, as in Paper II.

In summary, our analysis of the observed chromospheric spectra, is consistent with

$A_{\text{He}}=0.075$; furthermore, we were able to estimate the uncertainty range as 0.065–0.085 in at least one favorable case. The value $A_{\text{He}}=0.085$ – i. e. the “canonical” photospheric helium abundance (e. g.: Asplund et al. 2005)) – could therefore be marginally consistent with our data, since it results in He features which agree with the observations at the limit of our estimated errors.

A final note on measuring the helium abundance in the solar chromosphere: The set of lines we have used, together with an estimate of the EUV coronal back-radiation, is the *minimum necessary* to estimate A_{He} in chromosphere. No meaningful estimates, for instance, can be obtained using only the optical He I lines or the EUV resonance lines alone. But (as in Paper II, or in all cases considered here, except region D at 16:20 UT), even this set of lines may not be *sufficient* for an accurate determination of A_{He} . In particular, while the optical He I lines are usually well constrained by typical chromospheric lines such as Ca II K or $H\alpha$, the resonance He I 58.4 line must also be constrained by lines forming in the lower transition region. In the high pressure environment of region D at the secondary peak of the EUV flare emission, this role is played by $H\alpha$. In other circumstances, additional constraints provided by other lines would be needed: intensities from other upper-chromospheric or lower-TR lines (e. g.: H I Ly- α); intensities from other He I and He II lines (e. g.: He II 25.6 nm); spectrally resolved profiles of the He I 58.4 and He II 30.4 lines. With the advent of more recent space missions, such as Hinode and its EUV spectrometer (EIS), and with the continued availability of the SOHO spectrometers (CDS and SUMER), there is now in fact a window of opportunity for obtaining stronger constraints for the kind of modeling described in this work.

This work was in part supported by a joint project CNR (Consiglio Nazionale delle Ricerche, Italy) and CONICET (Consejo Nacional de Investigaciones Científicas y Técnicas, Argentina). V. Andretta also acknowledges support by the Italian Space Agency (ASI) – contracts ASI/INAF I/035/05/0 and I/015/07/0.

We would like to thank the SOHO/CDS and NSO teams for their support in carrying out the observations analyzed in this paper. We are also grateful to R. Falciani and G. Cauzzi who acquired the data at NSO.

SOHO is a project of international cooperation between ESA and NASA. The NSO (National Solar Observatory, USA) is operated by the Association of Universities for Research in Astronomy, Inc. (AURA), under cooperative agreement with the National Science Foundation.

We finally thankfully acknowledge the efforts of the CHIANTI consortium members for making readily available and usable a fine code and database for astrophysical applications.

CHIANTI is a collaborative project involving the NRL (Naval Research Laboratory, USA), RAL (Rutherford Appleton Laboratory, UK), MSSL (Mullard Space Science Laboratory, UK), the Universities of Florence (Italy) and Cambridge (UK), and George Mason University (USA).

REFERENCES

- Andretta, V., Del Zanna, G., & Jordan, S. D. 2003, *A&A*, 400, 737
- Andretta, V., & Jones, H. P. 1997, *ApJ*, 489, 375
- Asplund, M., Grevesse, N., & Sauval, A. J. 2005, in *Astronomical Society of the Pacific Conference Series*, Vol. 336, *Cosmic Abundances as Records of Stellar Evolution and Nucleosynthesis*, ed. T. G. Barnes, III & F. N. Bash, 25–38
- Avrett, E. H., & Loeser, R. 1984, in *Methods in Radiative Transfer*, ed. W. Kalkofen (Cambridge: Cambridge Univ. Press), 341–380
- Cook, J. W., Keenan, F. P., Harra, L. K., & Tayal, S. S. 1994, *ApJ*, 429, 924
- Del Zanna, G., Landini, M., & Mason, H. E. 2002, *A&A*, 385, 968
- Delaboudinière, J.-P. et al. 1995, *Sol. Phys.*, 162, 291
- Dere, K. P., & Cook, J. W. 1979, *ApJ*, 229, 772
- Drake, J. J. 2003, *Adv. Space Res.*, 32, 945
- Falchi, A., & Mauas, P. J. D. 1998, *A&A*, 336, 281
- Feldman, U., Landi, E., & Laming, J. M. 2005, *ApJ*, 619, 1142
- Fludra, A., & Schmelz, J. T. 1999, *A&A*, 348, 286
- Fredvik, T., & Maltby, P. 1999, *Sol. Phys.*, 184, 113
- Geiss, J. 1982, *Space Sci. Rev.*, 33, 201
- . 1998, *Space Sci. Rev.*, 85, 241
- Gunár, S., Heinzl, P., Schmieder, B., Schwartz, P., & Anzer, U. 2007, *A&A*, 472, 929
- Harrison, R. A. et al. 1995, *Sol. Phys.*, 162, 233

- Hovestadt, D. et al. 1995, *Sol. Phys.*, 162, 441
- Killie, M. A., Lie-Svendsen, Ø., & Leer, E. 2005, *ApJ*, 632, L155
- Landi, E., Del Zanna, G., Young, P. R., Dere, K. P., Mason, H. E., & Landini, M. 2006, *ApJS*, 162, 261
- Mandzhavidze, N., Ramaty, R., & Kozlovsky, B. 1997, *ApJ*, 489, L99
- . 1999, *ApJ*, 518, 918
- Mauas, P. J. D., Andretta, V., Falchi, A., Falciani, R., Teriaca, L., & Cauzzi, G. 2005, *ApJ*, 619, 604 (Paper II), [arXiv:astro-ph/0412058](https://arxiv.org/abs/astro-ph/0412058)
- Mauas, P. J. D., Falchi, A., Pasquini, L., & Pallavicini, R. 1997, *A&A*, 326, 249
- Murphy, R. J. 2007, *Space Sci. Rev.*, 130, 127
- Pietarila, A., & Judge, P. G. 2004, *ApJ*, 606, 1239
- Share, G. H., & Murphy, R. J. 1998, *ApJ*, 508, 876
- Teriaca, L., Falchi, A., Cauzzi, G., Falciani, R., Smaldone, L. A., & Andretta, V. 2003, *ApJ*, 588, 596 (Paper I)
- Vernazza, J. E., & Reeves, E. M. 1978, *ApJS*, 37, 485
- Young, P. R., Del Zanna, G., Landi, E., Dere, K. P., Mason, H. E., & Landini, M. 2003, *ApJS*, 144, 135, [astro-ph/0209493](https://arxiv.org/abs/astro-ph/0209493)
- Zirin, H. 1975, *ApJ*, 199, L63

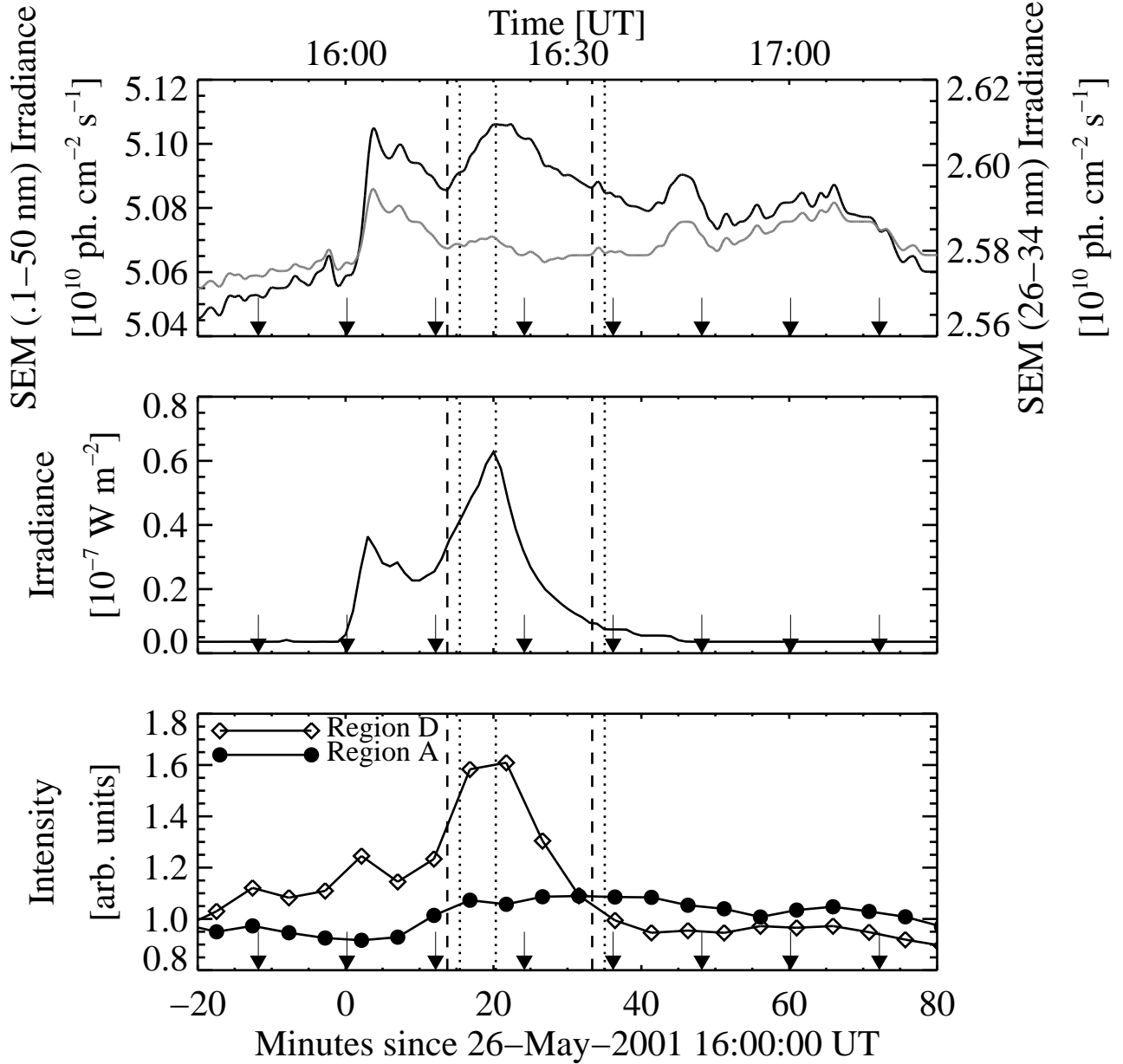


Fig. 2.— Light curves in the EUV and soft-X bands (1-minute resolution), before and during the C-class flare studied in this paper, compared with optical measurements. *Top panel:* EUV Irradiance at 1 AU, from SOHO/SEM (black: $\lambda < 50 \text{ nm}$; grey: $26 < \lambda < 34 \text{ nm}$); *Middle panel:* Soft-X irradiance from GOES-10 (0.05-0.4 nm band); *Bottom panel:* H α intensity observed at the Dunn Solar Telescope (DST) in the two representative regions analyzed in this paper (see Fig. 1). The vertical arrows mark the times of the full-disk images in the 19.5 nm band taken by SOHO/EIT during the *CME watch* observing program, while the vertical dashed and dotted lines mark the times of the spectra of regions A and D, respectively.

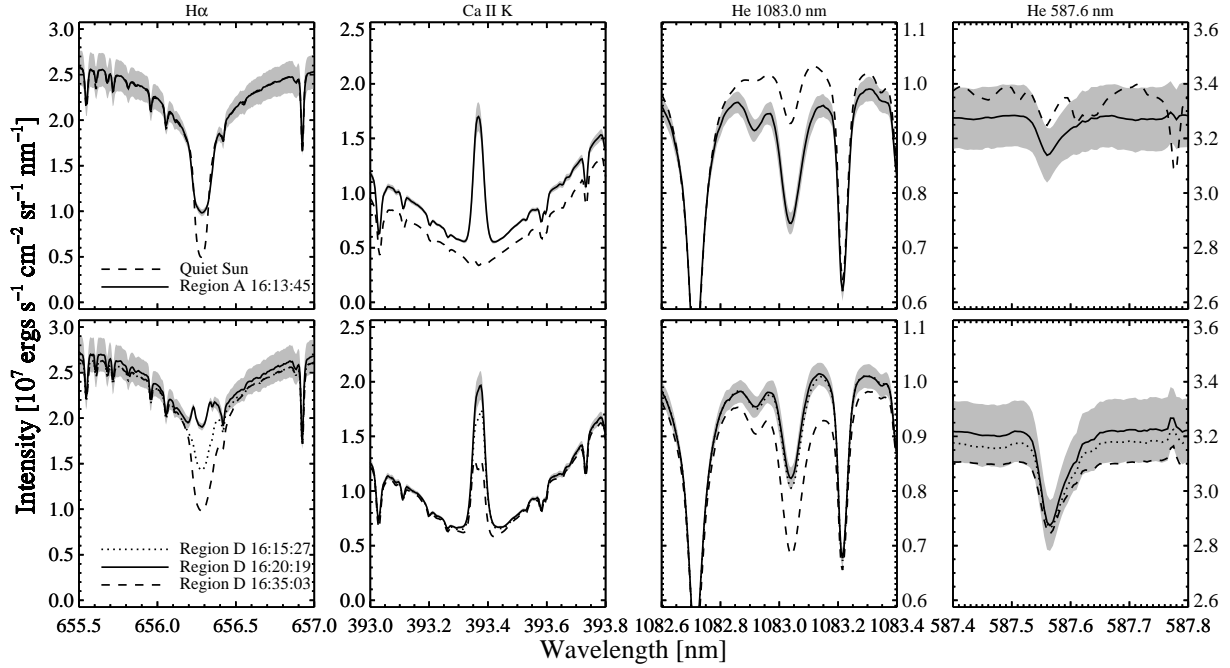


Fig. 3.— Profiles for the lines H α , Ca II K, He I 1083.0 and 587.6. *Top panels:* Observations in a quiescent, reference region (dashed lines) and in region A at 16:14 UT (solid lines). *Bottom panels:* Observations in region D at 16:15 (dotted lines), 16:20 (solid lines), and 16:35 UT (dashed lines). Error bands for the profiles in region A at 16:14 UT and region D at 16:20 UT are also shown. Note: telluric lines have been removed from the He I 587.6 profiles, except in the case of the reference region.

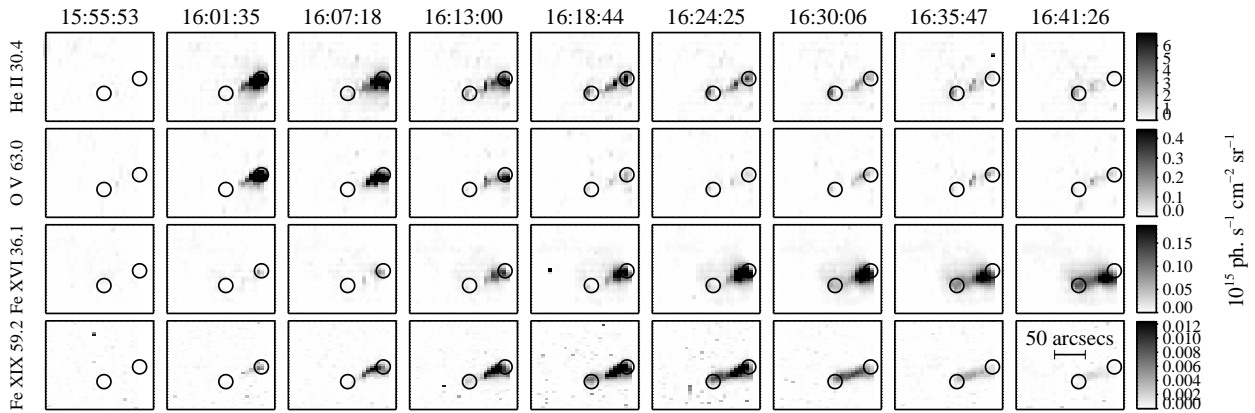


Fig. 4.— Sequences of CDS/NIS *residual* spectroheliograms showing, for about 40 minutes, the evolution of the event from its onset (at about 16:01 UT). The images obtained from the profiles of the He I 58.4 nm are very similar to those of the He II 30.4 nm line, and thus are not shown here. Circles mark the two regions of interest (A and D: left-most and right-most circles, respectively).

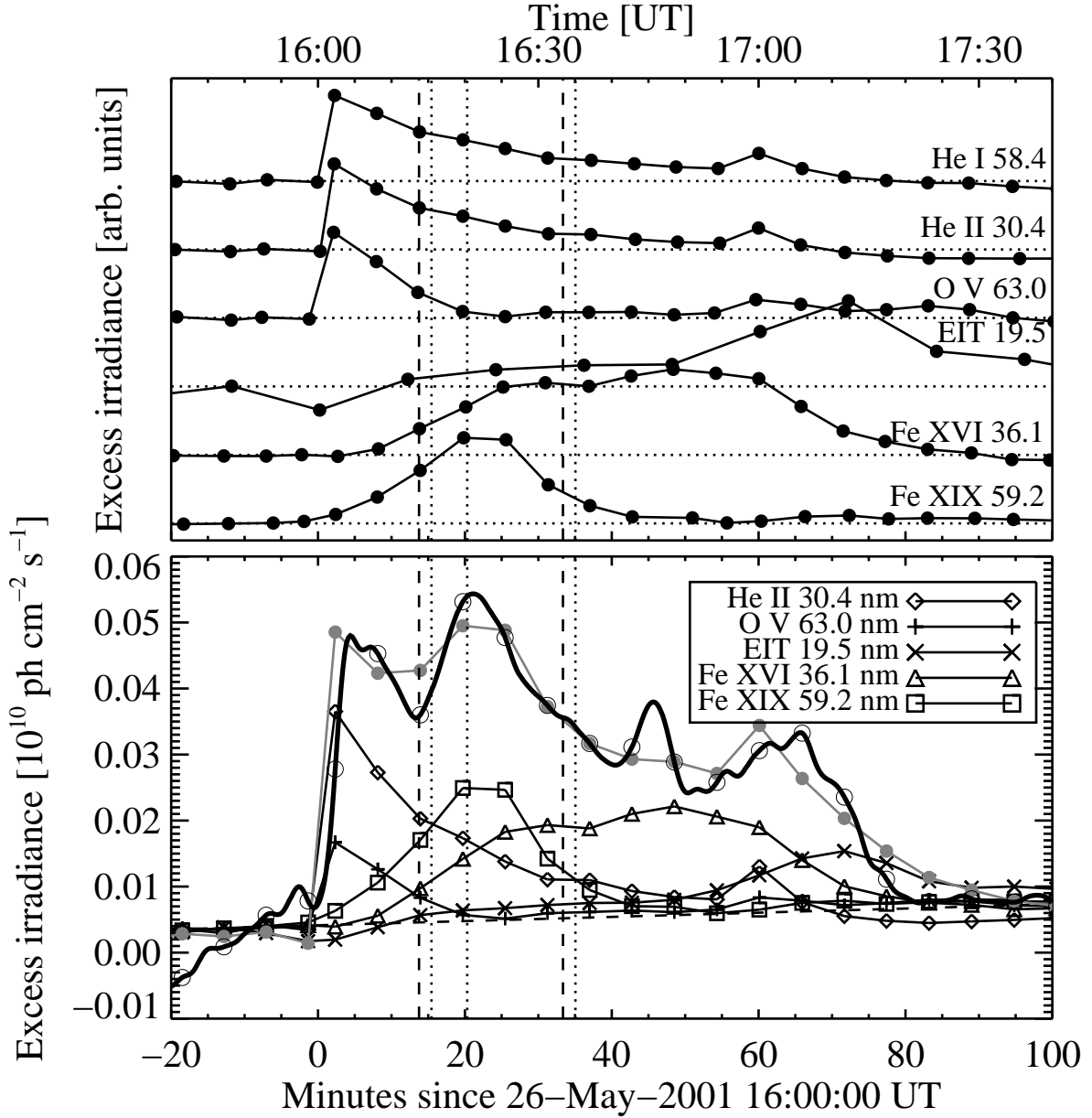


Fig. 5.— *Top panel:* Light curves of residual irradiances in CDS lines; the EIT enhancement over the flaring region is also shown. *Bottom panel:* Light curve of excess SEM_0 irradiance during the flare (black, thick line, and empty circles), compared with the fit (grey line, and filled circles) obtained by combining the CDS and EIT light curves. The vertical dashed and dotted lines mark the times of the spectra taken in regions A and D, as in Fig. 2.

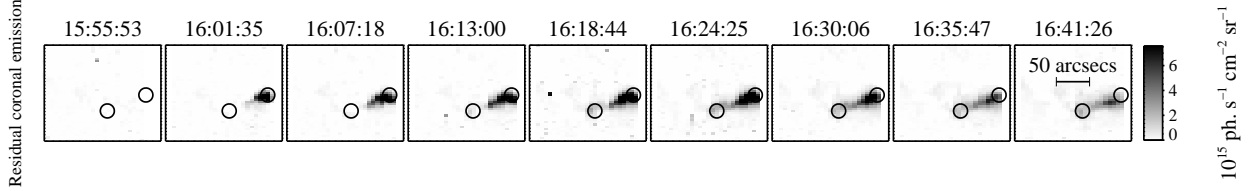


Fig. 6.— Sequences of images showing the variation of the *enhancement* of EUV illumination in the $\lambda < 50$ nm band, in the flaring area. Radiance maps shown with the same format as in Fig. 4.

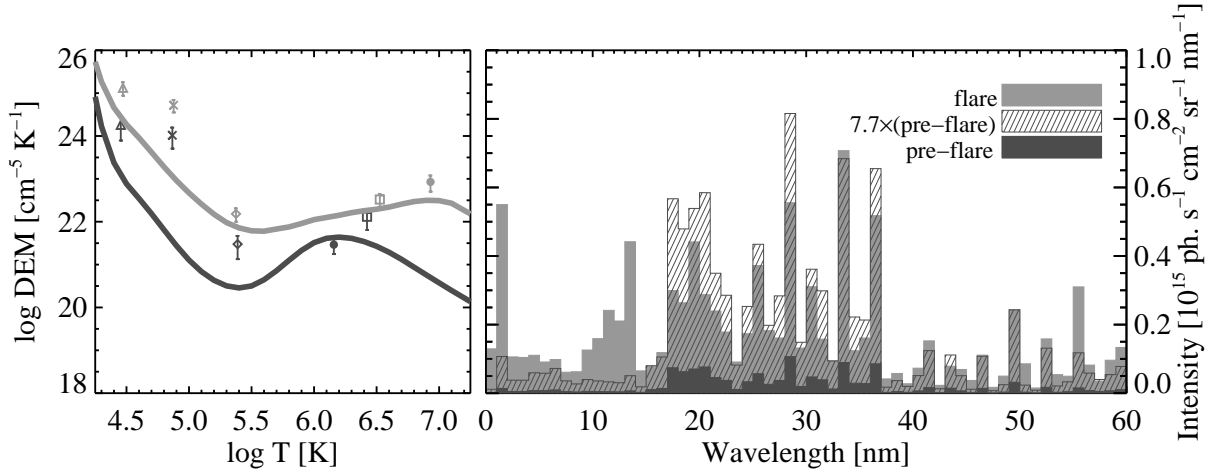


Fig. 7.— *Left*: DEM distributions for the “reference” AR atmosphere (black line) and the flaring region D at 16:20 UT (grey line, yellow in the on-line version). The observed intensities (multiplied by the factor $\text{DEM}(T_{\text{eff}})/I_{\text{calc}}$) are also shown for the various CDS lines: He I 58.4 nm (triangles), He II 30.4 nm (\times symbols), O V 62.9 nm (diamonds), Fe XVI 36.1 nm (squares), and the blend at 59.2 nm (filled circles). *Right*: Spectral distributions from the above DEMs, excluding all He I and He II lines and continua, compared with the “standard” AR emission times the multiplicative factor of ≈ 7.7 given in Table 1 (dashed histogram).

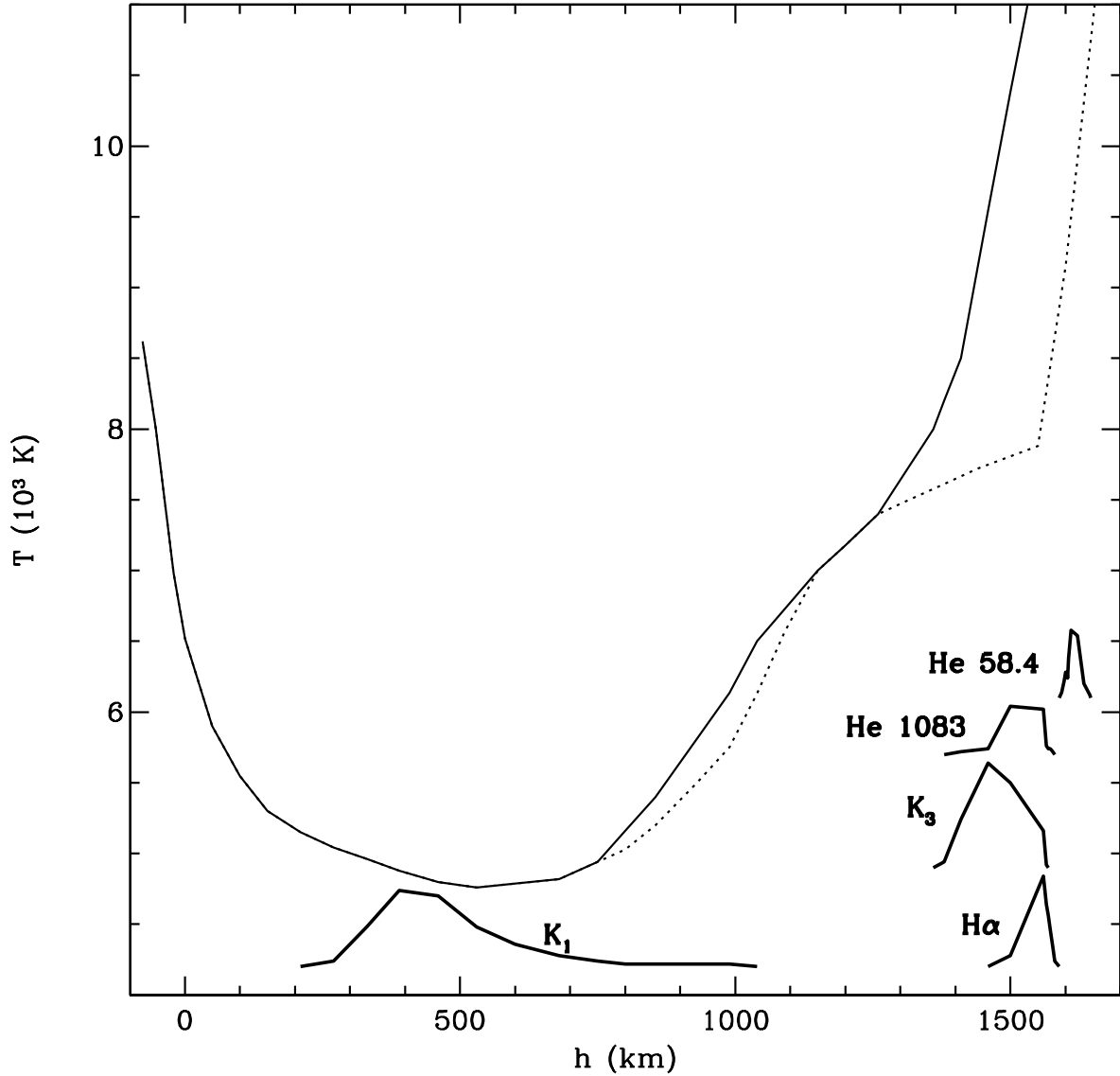


Fig. 8.— Region A: temperature versus height distribution (solid line) of the atmospheric model obtained for $A_{\text{He}}=0.1$. The model for the active region studied in Paper II (dotted line) is displayed for comparison. Also shown are the intensity contribution functions, in arbitrary units (solid, thick lines), of the different spectral features we used to build the model. The He I 587.6 contribution function is proportional to the one of the infrared He I line.

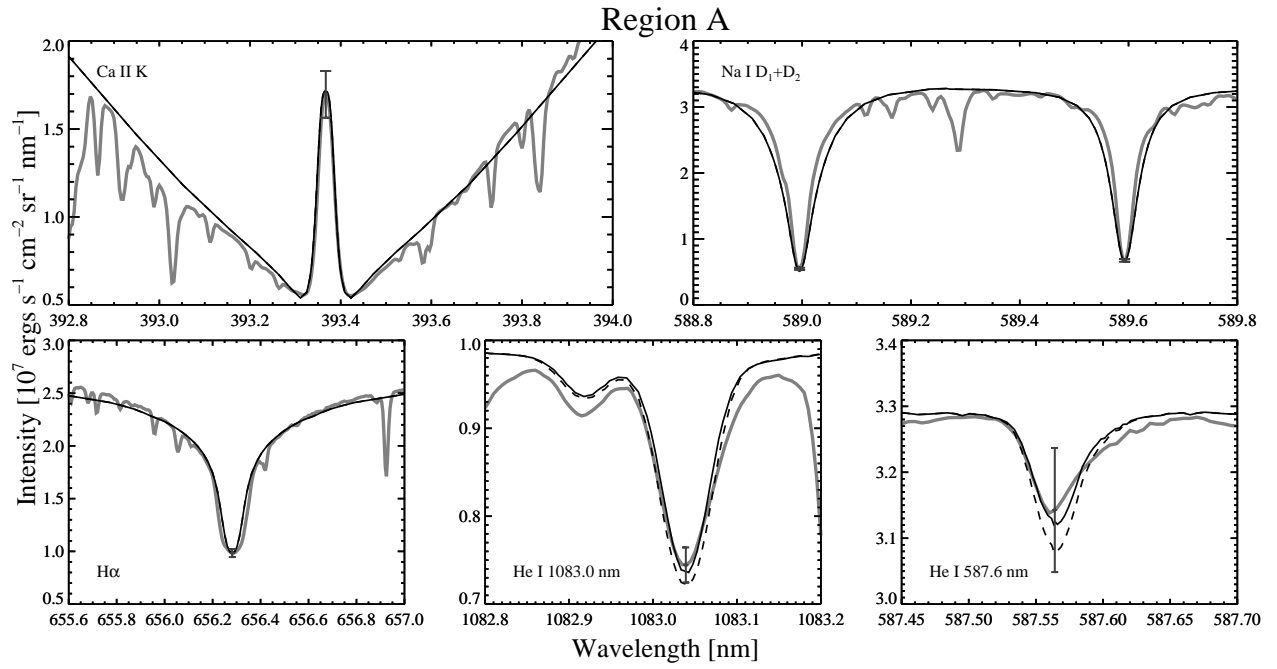


Fig. 9.— Region A: comparison between observed (thick grey line) and computed profiles (black lines). The solid and dashed lines indicate the profiles computed for the radiation determined at 16:14 and 16:33 UT, respectively.

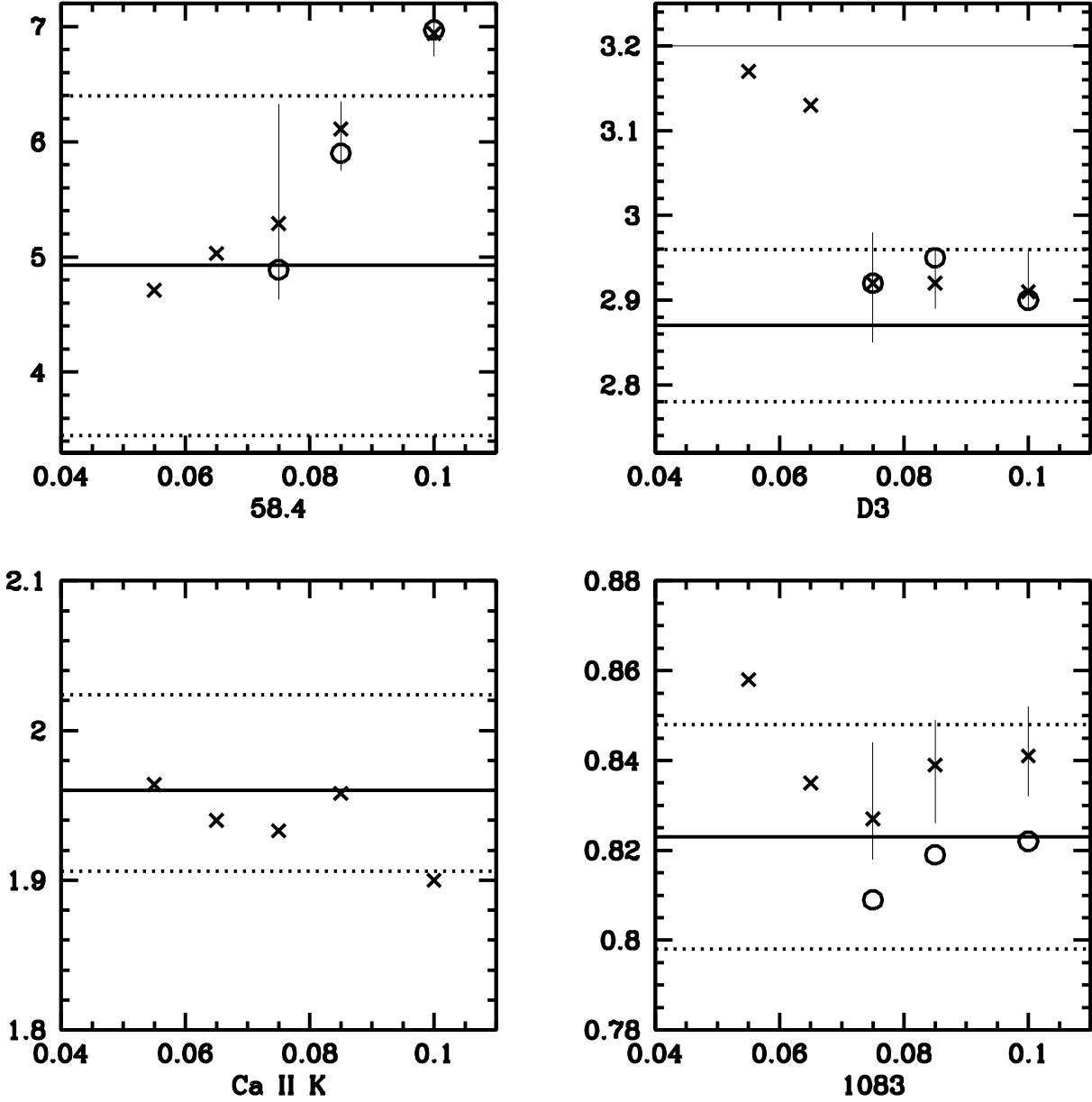


Fig. 10.— Computed radiance (10^4 ergs s $^{-1}$ cm $^{-2}$ sr $^{-1}$) and central line intensity (10^7 ergs s $^{-1}$ cm $^{-2}$ sr $^{-1}$ nm $^{-1}$) versus A_{He} . Radiance of the 58.4 line and the line center intensity of the D₃, 1083 and Ca II K lines are computed for the best-matching models obtained for region D at t_2 , with I_{cor} given in Table 1 and the scaled spectral distribution of the active region (crosses). Open dots indicate values obtained with the flare spectral distribution described Sec. 3.1. The thick line indicates the observed value and the dotted line its estimated uncertainty. The thin line indicates the continuum level for D₃.

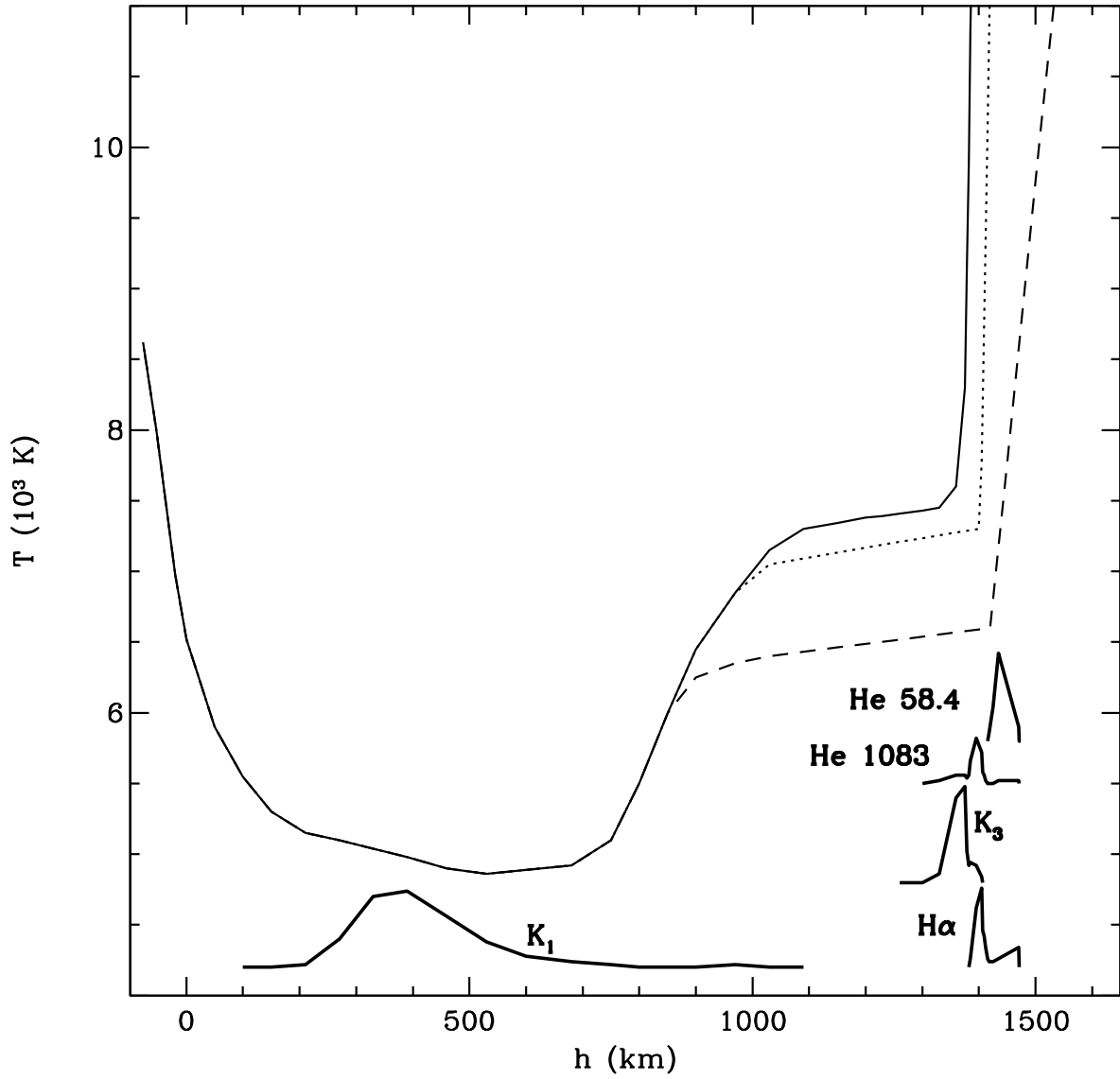


Fig. 11.— Region D: temperature versus height distribution of the atmospheric models obtained for $A_{\text{He}}=0.075$ at the considered times (dotted line: 16:15 UT, solid line: 16:20 UT, dashed line: 16:35 UT). Central intensity contribution functions of various lines are also shown, as in Fig. 8.

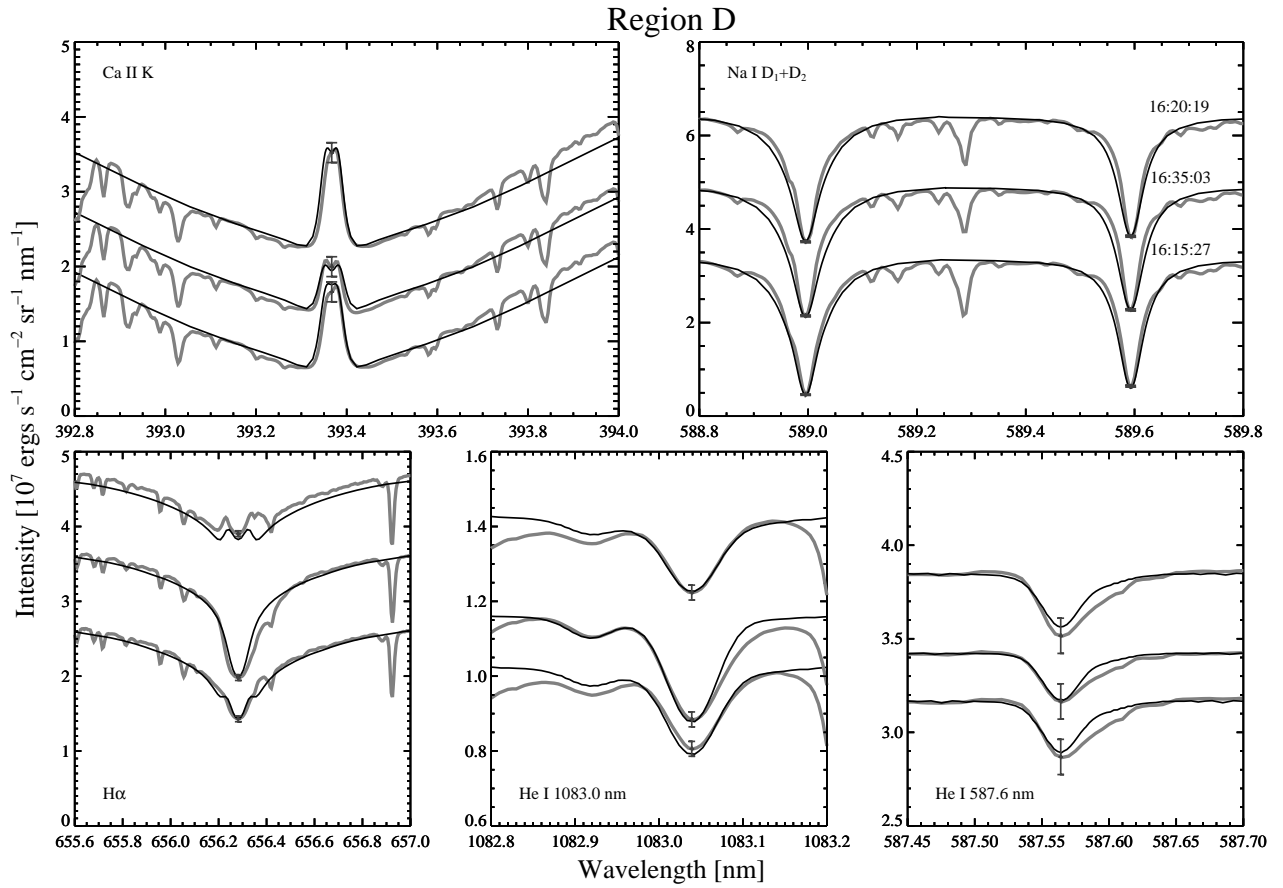


Fig. 12.— Region D: comparison between observed (thick grey line) and computed profiles (black line). The profiles at 16:35 and 16:20 UT are offset by an arbitrary, constant amount along the ordinate.

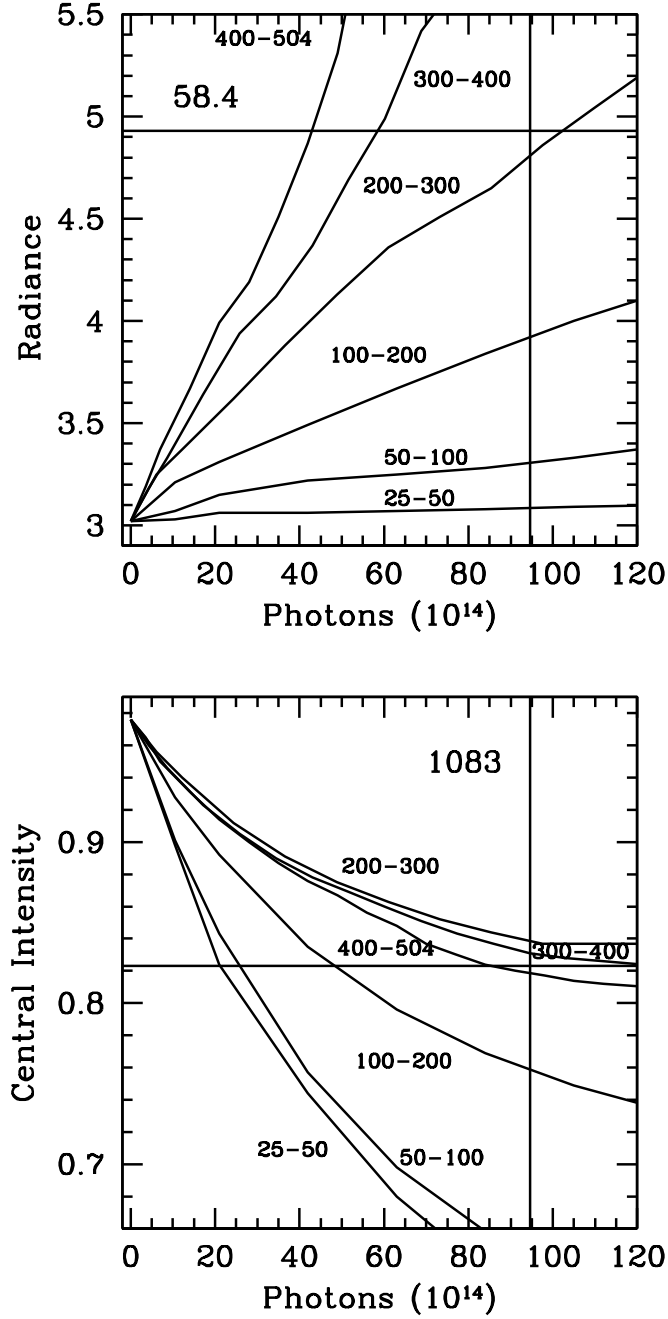


Fig. 13.— Radiance for the 58.4 nm line (top), and central intensity of the 1083 line (bottom), as a function of I_{cor} , for different step-like distributions of the field. Same units as in Fig. 10 for the ordinates; I_{cor} given in 10^{14} ph. s $^{-1}$ cm $^{-2}$ sr $^{-1}$. The vertical line marks the value of I_{cor} at t_2 , while the horizontal lines indicate the mean value of the measured 58.4 nm radiance (top panel) and 1083 nm central intensity (bottom panel).